

# The Position and Nature of Bluff Body Aeroacoustic Sources

## An Experimental Investigation

*University of Bristol Experimental Methods for Aerodynamics and Aeroacoustics 2024*

Matthew Bell, 10<sup>th</sup> December 2024

### Abstract

*This paper aims to discover whether acoustic pressure waves are a significant factor in Vortex-Induced Vibration. The dominant acoustic source in the wake of a cylinder in  $Re = 36,000$  flow is investigated, confirming the position and type of source in the wake. Particle Image Velocimetry techniques are used to characterise the flow and to compare observed velocity measurements to a theoretical dipole centred at the point in the wake with the highest Turbulent Kinetic Energy ( $T_{KE}$ ). Maximum  $T_{KE}$  is found exactly one diameter behind the cylinder's trailing edge and the velocity field is consistent with a dipole source at this point. Acoustic Power and Pressure Level spectra are collected in an aeroacoustic wind tunnel and compared to an idealised dipole, and some mediocre agreement between the model and measurement is found. The dipole is found to vibrate across the flow direction and thus is not anticipated to significantly contribute to vibrations, giving evidence that vibrations are the result of pressure fluctuations due to vortex shedding.*



University of  
**BRISTOL**

<b>Contents</b>					
<b>1</b>	<b>Introduction</b>	<b>4</b>	<b>Discussion</b>	<b>9</b>	
<b>2</b>	<b>Methodology</b>	<b>1</b>	<b>5</b>	<b>Conclusion</b>	<b>10</b>
<b>3</b>	<b>Results</b>	<b>2</b>	<b>References</b>	<b>11</b>	
		<b>6</b>	<b>Appendices</b>	<b>12</b>	

### Acronyms

$Re$	Reynolds Number	<b>PIV</b>	Particle Image Velocimetry
$St$	Strouhal Number	<b>PSD</b>	Power Spectral Density
$T_{KE}$	Turbulent Kinetic Energy	<b>SE</b>	Standard Error
$V$	Transverse Flow Velocity	<b>SPL</b>	Sound Pressure Level
<b>CI</b>	Confidence Interval	<b>VIV</b>	Vortex-Induced Vibration

## 1 Introduction

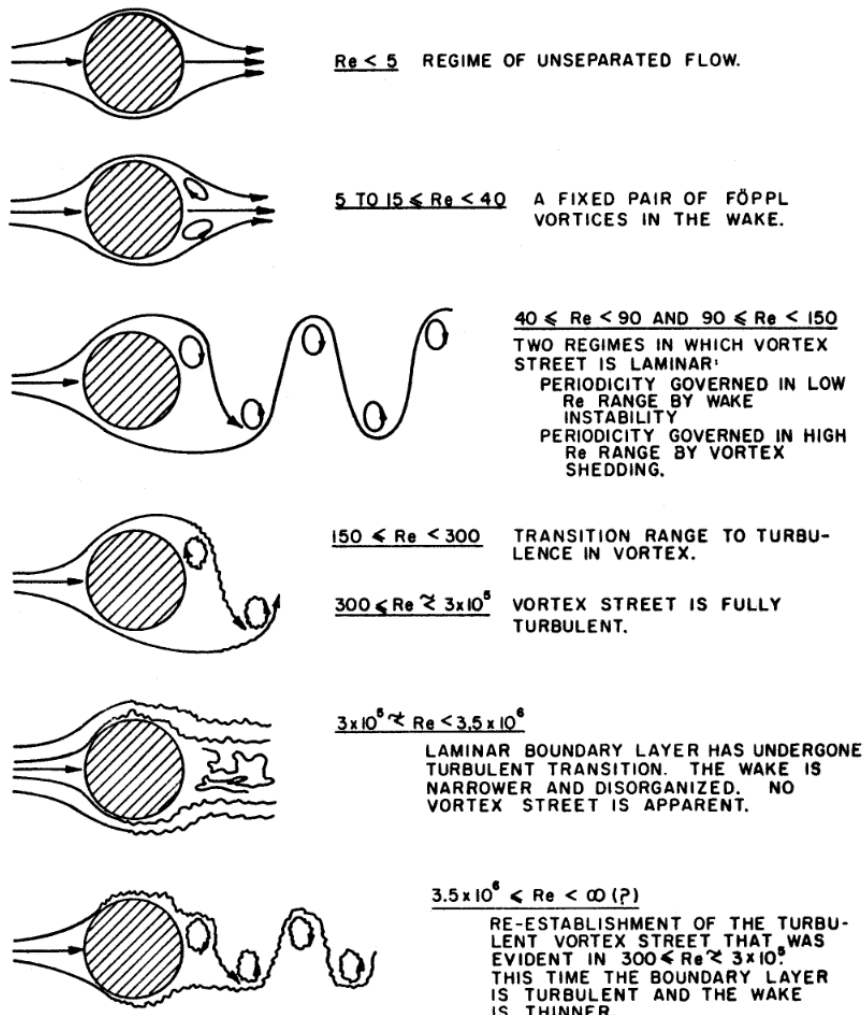


Figure 1: Regimes of Fluid Flow across Circular Cylinders [1]

In aerodynamics, a "bluff body" refers to any non-lifting body in a fluid flow. Sizes and shapes of bluff bodies can vary: from a radio antenna on a car driving down the motorway to skyscrapers in the windy atmosphere. Fluid flows over any body result in inertial forces from particle velocity changes and viscous forces from the "stickiness" of the flow across the body's surface [1][2], and the ratio of inertial to viscous forces is expressed as the Reynolds Number ( $Re$ ), a function of free-stream velocity ( $U_\infty$ ), body length ( $L$ ) and dynamic viscosity ( $\mu$ ):

$$Re = \frac{\text{inertial}}{\text{viscous}} = \frac{U_\infty L}{\mu} \quad (1)$$

As body size and flow speed increase, so does the Reynolds number, and this results in a turbulent wake for most real-life structures and wind speeds, as shown in Figure 1. Thus, this paper will focus on high- $Re$  flows, with Reynolds number above the  $Re= 300$  turbulent transition. Turbulent flows are characterised by periodic velocity and pressure fluctuations [3]. These pressure fluctuations propagate through the surrounding fluid and can be heard as noise or as clear tones in the case of musical instruments [3]. Early experiments by Dr Strouhal [4] focused on the noise made by wires in airflow. The belief at the time was that the drag force on the wires generated periodic forwards and backwards oscillations in the wire. Rayleigh's subsequent research [5] concluded that the direction of vibration was in the transverse flow direction, not in line with the flow. This vibration would be expected to create an acoustic dipole, the type of sound source you would hear from one arm of a tuning fork [6]. Successive studies have led to an understanding of "vortex shedding" in certain flow regimes,

where vortices (regions where flow encircles a point or line) of equal strength and alternating direction are shed periodically in the wake of a bluff body [1]. Modern investigations have found that this transverse Vortex-Induced Vibration (VIV) can cause damaging oscillatory motion if the frequency of vortex shedding approaches the natural vibratory frequency of the bluff body, a phenomenon called "lock-in" or "synchronization" [7], but it is unclear whether these vibrations are a result of the surface pressure on the body or as a result of pressure waves from acoustic sources in the wake. A cylinder is a common bluff body example with applications in heat exchangers [8] and thermowells in modern power stations and petrochemical plants, as well as aircraft landing gear and antennae [7]. In all these applications, harmonic oscillations due to acoustics must be avoided to mitigate the risk of damage from resulting vibrations, and this makes the cylinder an important subject to study. This paper aims to experimentally determine the position and nature of the main acoustic source in a high- $Re$  cylinder wake using Particle Image Velocimetry (PIV), and to compare the theoretical dipole source to pressure data collected with a far-field microphone array in an anechoic wind tunnel, in order to make inferences about the effect of the acoustic source on undesirable cylinder oscillations.

## 2 Methodology

### 2.1 Particle Image Velocimetry

PIV was used to gain insight into the flow structures, energy dissipation, and behaviour of the cylinder wake. As stated prior (Section 1), the objective was to determine the position and orientation of the acoustic source(s) in the wake and this can be done by calculating the time-averaged Turbulent Kinetic Energy ( $T_{KE}$ ) distribution in the wake and inspecting the time-averaged velocity fields using PIV measurements. A schematic of the laser and camera setup can be found in Figure 2, with the wind tunnel and test section dimensions found in Figure 5.

The flow was seeded with particles, and a laser sheet was shone vertically across the flow at the midpoint of the cylinder, to illuminate a plane of particles in the central plane of the flow. A camera was used to capture 2000 images of these particles at a frequency  $f = 840$  Hz. The brightest pixels in the image denote a particle's centre position, and without Gaussian peak fitting the maximum achievable precision was 1 px. Splitting each image into square "windows" and auto-correlating particle positions, the average particle position in each window was found. Comparing this position vector at time  $t$  and  $t + \frac{1}{f}$  allows the instantaneous velocity vector to be calculated for each window. A multi-pass windowing method was chosen, with a final window size of  $32 \times 32$  px and a 50% overlap. This produced a vector resolution of  $150 \times 120$  for the entire 2048 px square image, with some image cropping applied to isolate the flow region of interest. This resulted in a spatial resolution of approximately 1.14 vectors per mm after calibration.

Spatial calibration was achieved by holding a ruler in the laser sheet and taking an image on the camera. By ensuring the ruler was immersed in the laser sheet, out-of-plane measurement errors were mitigated, but the use of a ruler resulted in a spatial bias of  $\pm 0.5$  mm. For the full 132 mm image width, this translated to a spatial uncertainty of  $\pm 0.4\%$ .

The time domain uncertainty (random errors in sampling frequency) was not measured. Overall Standard Error (SE) can be conservatively estimated using the "bootstrap" method [9]. By randomly resampling velocity measurements and recombining into a larger sample, an estimate can be found for the mean velocity and SE measurement at one point in the flow. This is not perfect, as velocity variation is a natural consequence of the flow instability, and does not necessarily imply the measurement instruments have a large random error. Using this bootstrap method at a point in the flow which experiences little turbulence, shown in Figure 3, a mean velocity of  $28.00 \text{ ms}^{-1}$  and SE of 0.47 was calculated. 2000 bootstrap samples were generated from the 2000 original samples, ensuring a large sample size and statistical convergence [10]. This approach resulted in a conservative 95 % Confidence Interval (CI) of  $28 \pm 0.92 \text{ ms}^{-1}$ , or  $\pm 3\%$ , for single direction velocity components. Velocity error was assumed to be equal in both directions, which is conservative as it is likely to be higher in the streamwise direction due to the higher average flow speed.

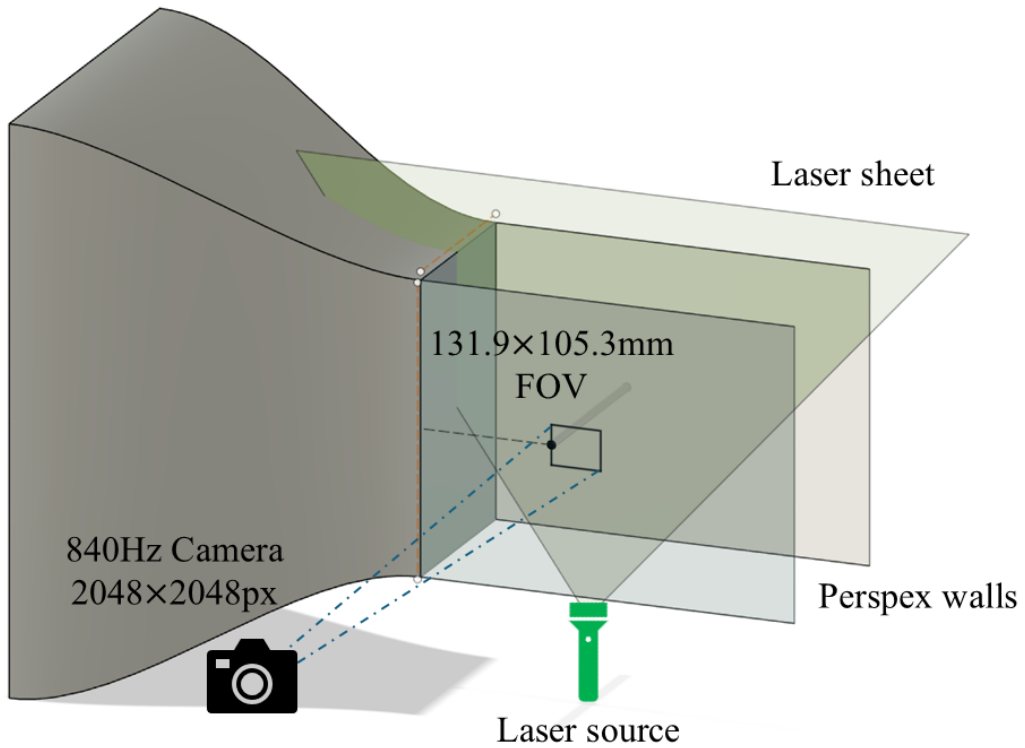
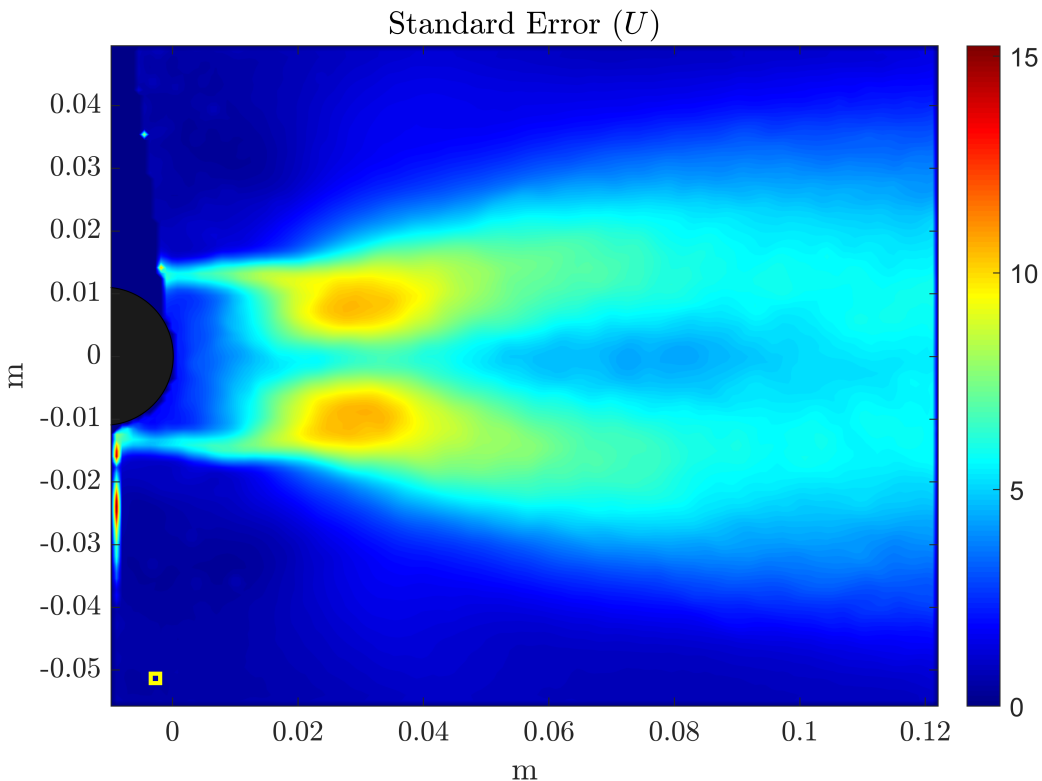


Figure 2: Schematic of PIV Technique


 Figure 3: SE for velocity component  $U$ , with the bootstrap interrogation point plotted as a yellow square

To achieve the aim of this paper, the  $T_{KE}$  was calculated at every point in the flow using Equation (2) for all 2000 samples, and the time-averaged  $T_{KE}$  field was found. The point of maximum average  $T_{KE}$

was taken as the location of the strongest acoustic source in the flow, and this was used to create a theoretical model of the ideal dipole source in the wake. Time-averaged velocity fields were also calculated and used to determine the nature of the source in the wake.

$$T_{KE} = \frac{1}{2}(u^2 + v^2 + w^2) \quad (2)$$

where  $u$ ,  $v$ , and  $w$  are defined as the local flow speed:

$$u = U - U_\infty \quad (3)$$

where  $U_\infty$  is the freestream flow velocity and  $U$  is the measured streamwise velocity, and the same can be done for  $v$  and  $w$ . This is important in the study of turbulence as it changes the frame of reference and removes the contribution of freestream velocity to allow a clearer mathematical definition of the eddies and energy involved in turbulence. The propagated uncertainty for  $T_{KE}$  measurements was then 6 %, shown by Equation (A-4) in Section A.

## 2.2 Pressure Measurements

In order to compare the theoretical sound source to the observed phenomenon, pressure measurements were taken to determine the frequency and radiated acoustic power from the turbulent flow over the cylinder. To obtain these measurements, the Kevlar-walled aeroacoustic wind tunnel at the University of Bristol was used. Detailed information on the wind tunnel design can be found in [11]. A schematic of the experimental setup is shown in Figure 5, alongside an image of the test section.

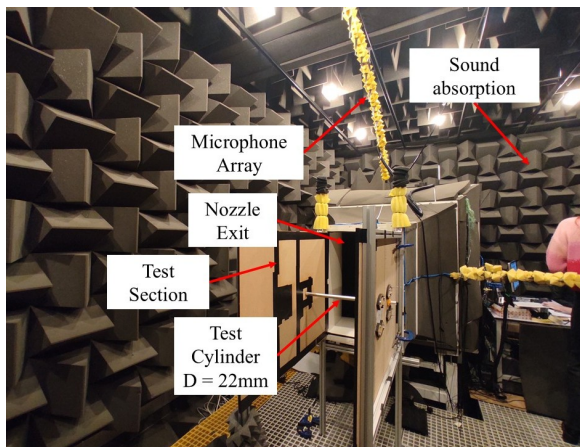


Figure 4: Wind Tunnel Test Section

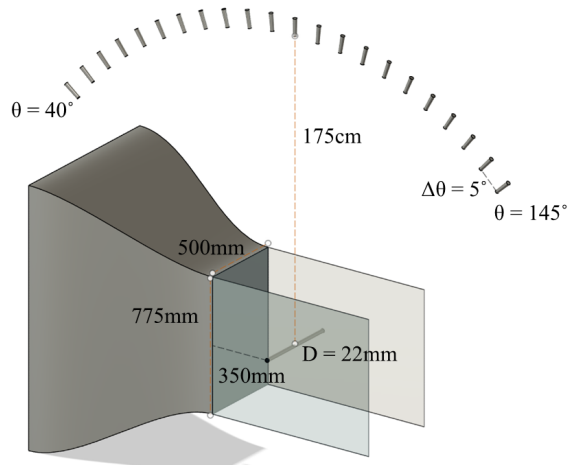


Figure 5: Schematic of the Anechoic Wind Tunnel Setup

The aeroacoustic wind tunnel is anechoic for frequencies above 160 Hz [12], and the microphones used have a frequency range of 10 Hz-20 kHz [13]. As such, the minimum frequency for valid data collection was limited by the facility's design and not by the microphones. The peak amplitude frequency recorded in Section 3 fell within the flat frequency response of the microphones, and a graph of this frequency response can be found in Figure B-1. Prior to experimental measurements each microphone was calibrated, using the appropriate pistonphone, and the sensitivity was recorded in order to convert mV readings into Pa. To achieve the desired flow regime ( $Re > 300$ ) at the ambient temperature of approximately 20 °C, a cylinder with 22 mm diameter and flow speed of 24.99 ms<sup>-1</sup> was selected. Pressure data from each microphone were sampled at a frequency of 65 kHz (2<sup>16</sup>Hz) for 10 seconds, and Power Spectral Density (PSD) was estimated using Welch's method [14], with a 90 % overlap and Hanning window size of 2<sup>13</sup>. The Sound Pressure Level (SPL) ( $L_P$ ) distribution was then calculated using Equation (4) [6]:

$$L_P = 10 \log_{10} \left( \frac{P}{p_{ref}^2} \right) \quad (4)$$

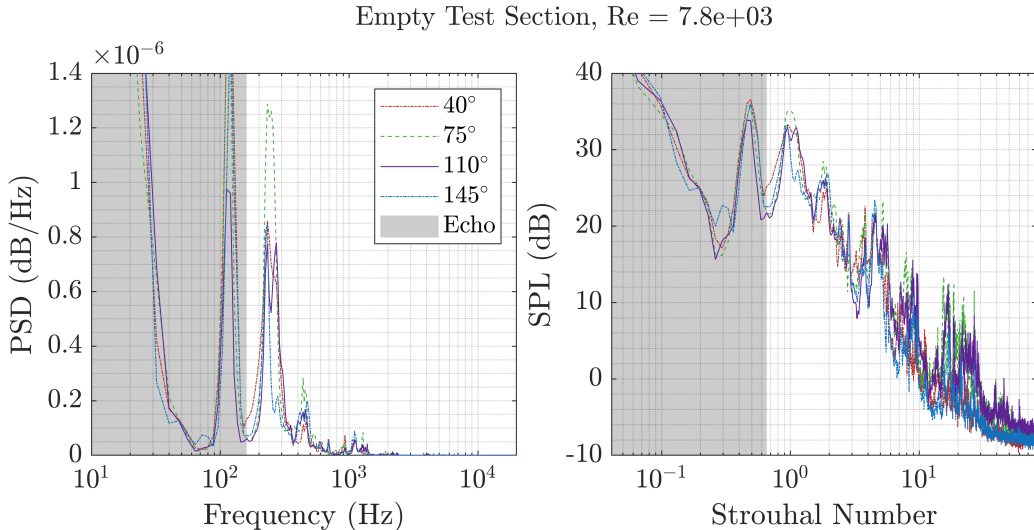


Figure 6: Pressure data recorded for an empty test section at a flow speed of  $5.4 \text{ ms}^{-1}$

where  $P$  is the PSD at that frequency and  $p_{ref}$  is  $20 \mu\text{Pa}$ . Prior to measuring the cylinder noise, the wind tunnel noise with an empty test section was recorded, to validate the later results and prove that the recorded noise was resulting from the cylinder and not from the wind tunnel jet mixing with the free air in the chamber. This measurement is presented in Figure 6.

Strouhal Number ( $St$ ) is defined in Equation (5) [1]:

$$St = \frac{fD}{U_\infty} \quad (5)$$

A theoretical dipole radiates pressure waves with amplitude given by [6]:

$$|p(r, t, \theta)| = \frac{Q\rho ck}{4\pi r} kd \cdot \cos(\theta) = \frac{1}{r} \cdot a \cdot \cos(\theta) \quad (6)$$

$Q$ ,  $k$ , and  $d$  are all constants: properties of the acoustic source. Density,  $\rho$ , and wave speed,  $c$ , are also assumed to be constant due to the low Mach number ( $M \approx 0.07$ ) flow in the wind tunnel, and the equation is simplified to the form on the right hand side where  $a$  combines all the constants into one unknown and  $r$  is the radius of the microphone from the source. In this investigation the acoustic source's properties were unknown, so the constant  $a$  was found through a least squares regression, attempting to fit the ideal dipole's radial pressure distribution in Equation (6) onto the experimental results. Corrections were made to the  $r$  value to account for the observed position of the dipole from the PIV experiment, in a simplified version of Lighthill's acoustic analogy [3]. The most important distinction to Lighthill's analogy is the assumption that density, and thus wave speed, is constant in the cylinder wake. As a result, this simple dipole model will not capture the distortion from the turbulence made by the jet mixing with the stagnant air at the nozzle exit, and is likely to underestimate the dissipation from this mixing. The full set of equations and derivations can be found in Section C. Experimental uncertainty was estimated based on the parameters used in Welch's method. Based on the microphone manufacturer's specification [13], the microphone's error was deemed negligible, as the recorded frequencies corresponding to peak PSD are in the flat frequency response of the microphones shown in Figure B-1. The uncertainty in the PSD calculation was estimated to be  $\pm 3.5\%$ , which results in an SPL error of 3%. The full derivation can be found in Section A.

### 3 Results

#### 3.1 Particle Image Velocimetry

Below are the time-averaged  $T_{KE}$  and Transverse Flow Velocity ( $V$ ) fields in Figure 7 and Figure 10, with flow travelling from left to right on the page. The peak  $T_{KE}$  of  $551 \text{ m}^2\text{s}^{-2}$  was found 22 mm, exactly 1 cylinder diameter, behind the cylinder's trailing edge. Peak  $T_{KE}$  was vertically in line with the cylinder, as expected. At this point, the measured average  $V$  was  $0.02 \text{ ms}^{-1}$ , near zero as expected, and the streamwise flow was reversed, with  $u = -30.78 \text{ ms}^{-1}$  (as defined in Equation (3)).

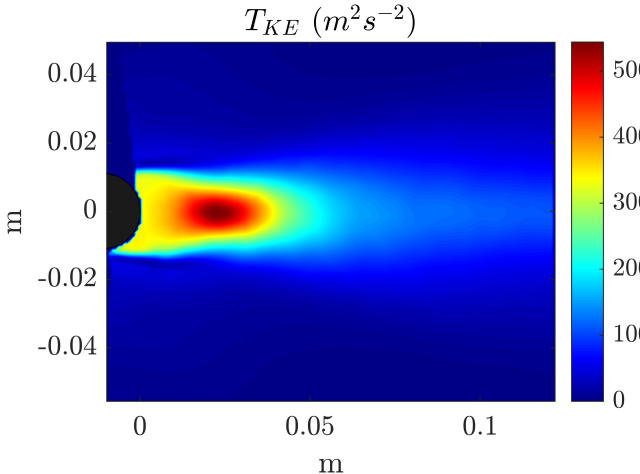


Figure 7: Time-Averaged  $T_{KE}$  Field

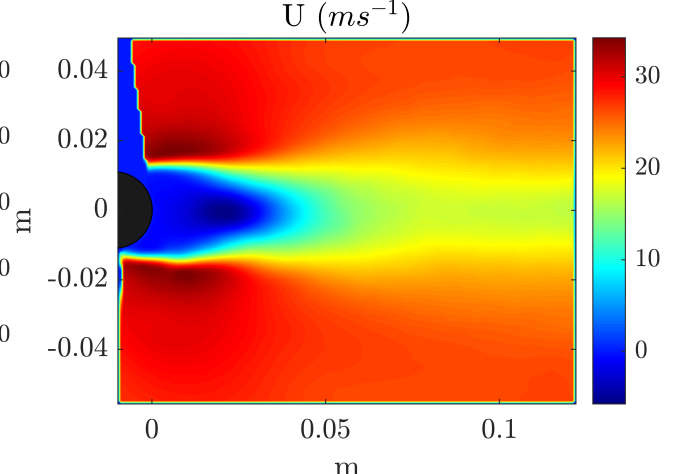


Figure 8: Time-Averaged Transverse Velocity Field

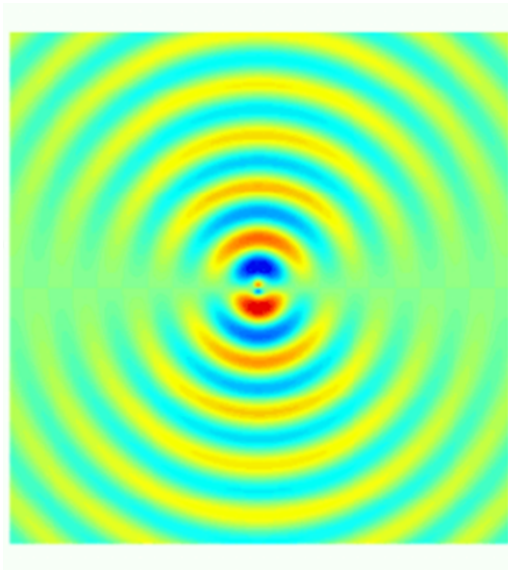


Figure 9: General Shape of Ideal Dipole Pressure Fluctuations [15]

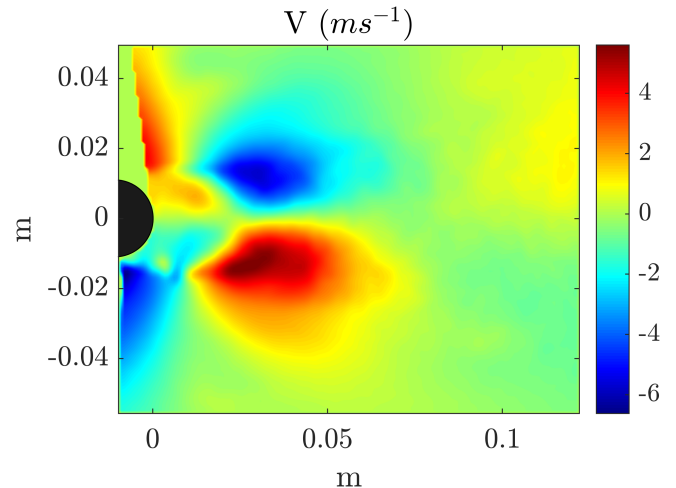


Figure 10: Time-Averaged Transverse Flow Velocity Field

The observed Transverse Flow Velocity field was, as expected, indicative of a dipole noise source like in Figure 9, with inwards-oriented average velocities above and below the maximum  $T_{KE}$  point. The velocity field could also have been that of a quadrupole noise source, due to the velocities above and below the cylinder surfaces, but the Streamwise Flow Velocity field in Figure 8 disagreed with this conclusion as there was no indication of periodic streamwise velocity oscillation centred at 22 mm behind the cylinder's trailing edge, and the pressure measurements in Figure 13 confirmed this was not a quadrupole.

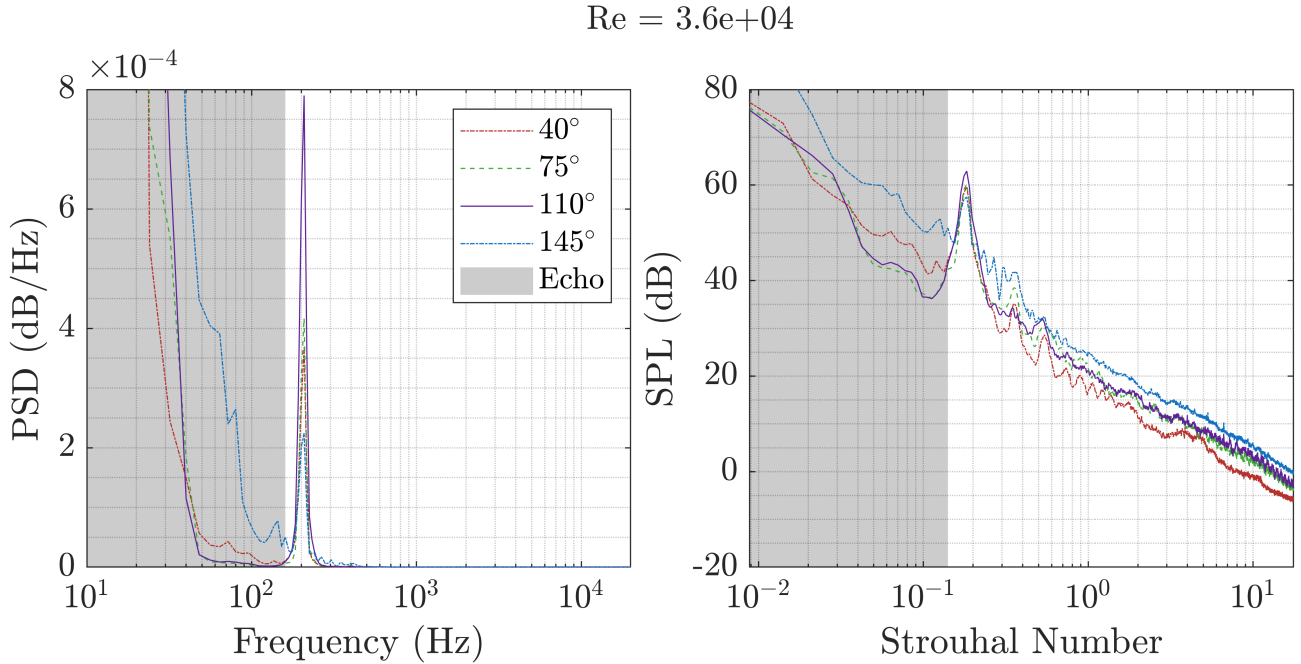
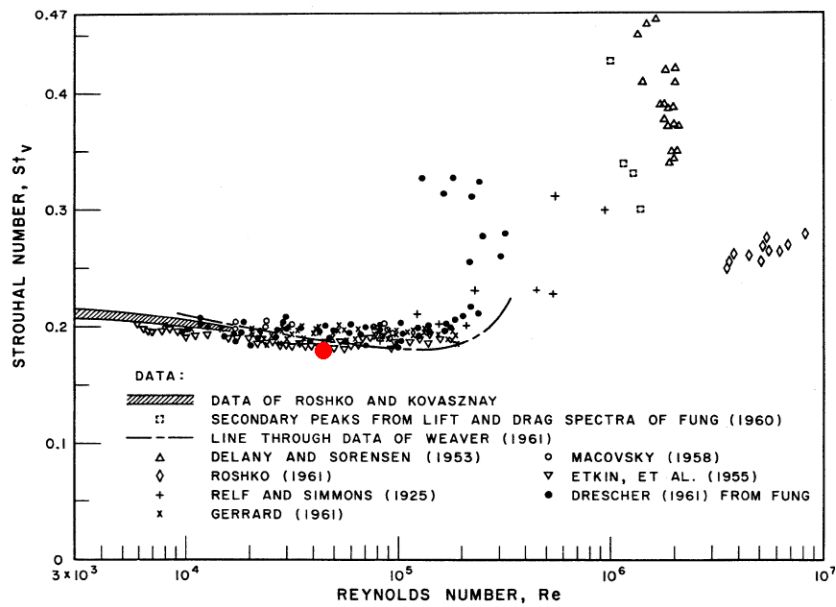


Figure 11: Power Spectral Density and Sound Pressure Level in Frequency Domain

### 3.2 Pressure Measurements

Measured PSD from four equally spaced microphones is presented in Figure 11, shown alongside the dimensionless equivalent, SPL, plotted against Strouhal number. For the calculated Reynolds number of  $Re = 3.6 \times 10^4$ , maximum power was radiated at a frequency of 208 Hz, corresponding to 57.5 dB at a Strouhal number of 0.18. The entire frequency range of the microphone is plotted, and the shaded region represents measurements where  $f \leq 160\text{Hz}$ . These frequencies were considered invalid due to the anechoic frequency range of the wind tunnel [11], as described in Section 2, but are plotted for the interest of the reader. The Strouhal-Reynolds number relationship agreed with existing research, and is plotted as the red dot on Figure 12.


 Figure 12: Comparison of Calculated  $Re$  and observed  $St$  [1]

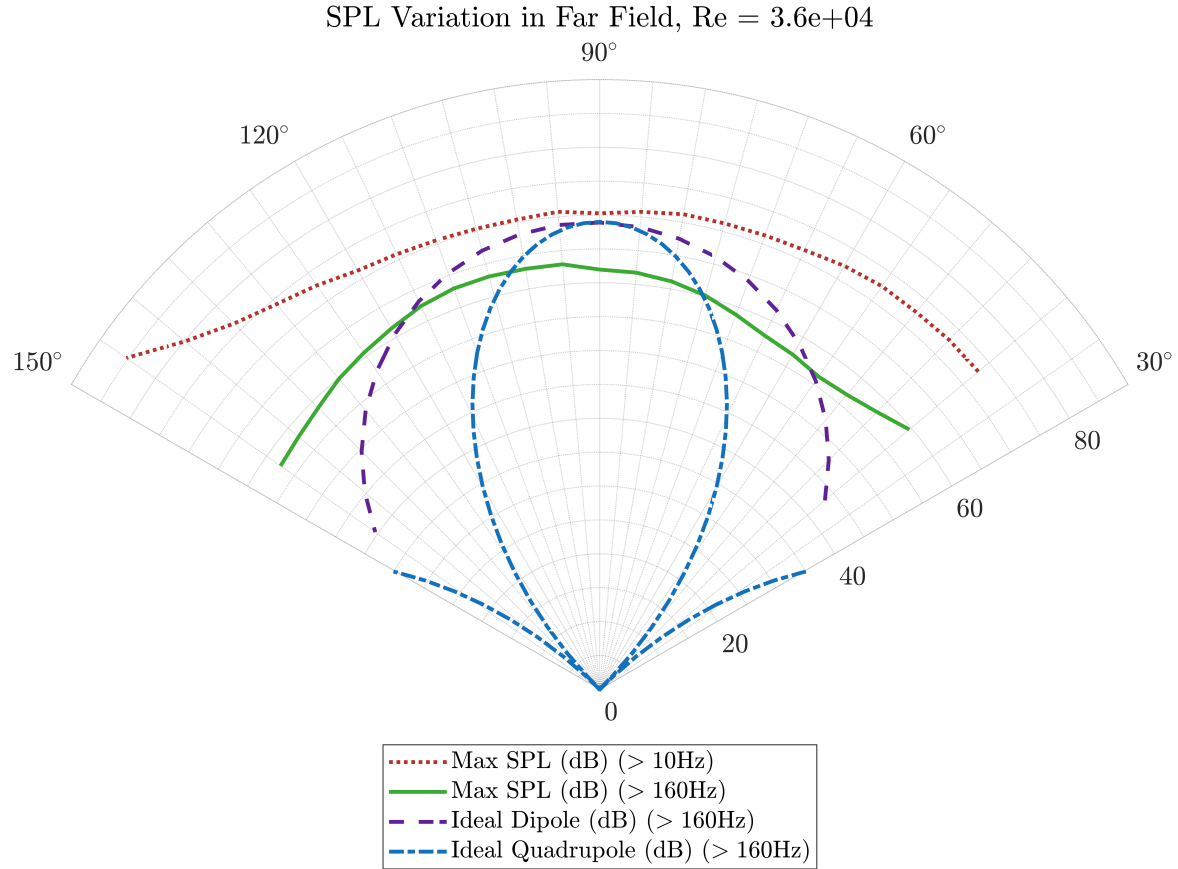


Figure 13: Measured vs Theoretical Sound Power Level

SPL variation with microphone position is plotted in Figure 13. This was key in determining the acoustic source's type and orientation. The result for frequencies less than 160 Hz was suspect, as these frequencies were reflected by the walls of the wind tunnel, so the measured power was overestimated for these frequencies. They are plotted for the reader's interest, but not used in the analysis of the acoustic sources. Peak SPL was found at 105°, disagreeing with the ideal dipole's 90° estimation, and the shape of the theoretical dipole's polar SPL distribution was similar but did not match the measured pressures. The theoretical dipole's SPL is plotted in Figure 14 and shows the cylinder's relative position, illustrating how a dipole at  $1 \cdot d$  behind the trailing edge would interact with the cylinder.

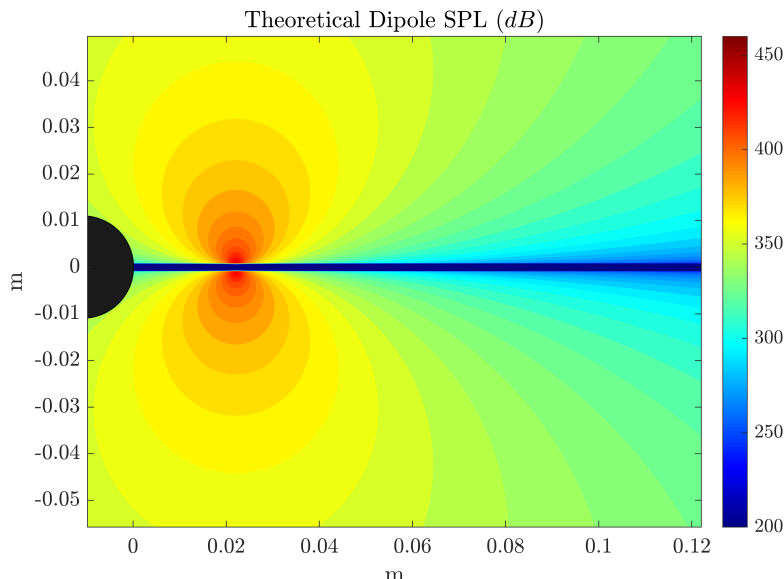


Figure 14: Theoretical Dipole SPL Distribution, Combining Equation (6) and Equation (4)

## 4 Discussion

Clearly, as shown in Figure 13, the corrections for distortion due to the freestream flow, and for the observed position of the dipole, were not sufficient to model the acoustic behaviour of the cylinder wake. The dipole's SPL varied more than the experimental measurements, which were more constant for a range of angles. This is consistent with the current understanding of high- $Re$  flows [16], where the turbulent structures are chaotic and there are a multitude of frequencies radiated by the turbulence in the wake, clearly demonstrated in Figure 11. The key assumption that the density (and thus the speed of sound) was constant throughout the turbulent flow could be inadequate for high Reynolds numbers. Another likely cause for the discrepancy was the fact that the wake was chaotic and did not just generate one acoustic source. In high- $Re$  regimes, there are many turbulence scales affecting the flow and radiating pressure waves as they are shed, and as they combine and grow downstream. Considering the wake noise as a single acoustic source was an oversimplification and resulted in poor agreement to the experimental data, because noise dissipation in the mixing region between the nozzle exit and the stagnant far field was not accounted for. Lighthill's acoustic analogy [3] remains the preferred method for predicting aeroacoustic noise in high- $Re$  flows, as turbulence scales are captured within a control volume and radiated to the far field.

There was, on the other hand, sufficient data to support the hypothesis that the main acoustic source in the wake was a dipole. The measured polar SPL variation in Figure 13 had the same general shape as a theoretical dipole, with less directivity. Importantly, the PIV results clearly indicated that the source was a dipole and gave an interesting result that peak  $T_{KE}$  was  $1 \cdot d$  behind the cylinder's trailing edge. This distance could warrant further study to see if and how it varies with  $Re$ . Due to the lack of directivity in the far-field measurements, it was not possible to confirm the source's position using microphone pressure measurements. Future studies could consider using a beamforming approach to locate the main acoustic source using pressure measurements as in [17]. Due to the theoretical dipole's position and orientation, shown in Figure 14, the cylinder was found to sit in the direction where less power is radiated by the dipole. Although there is some interaction with the acoustic waves, this implies that undesirable vibrations described in Section 1 would not be a consequence of the acoustic source's pressure waves, but would in fact be due to the periodic surface pressure fluctuations as vortices are shed into the wake.

## 5 Conclusion

In order to determine the position of the main acoustic source in a turbulent cylinder wake ( $Re = 36,000$ ) with Strouhal number  $St \simeq 0.18$ , the distribution of  $T_{KE}$  in the wake was measured using PIV. With a  $T_{KE}$  uncertainty of 6 %, the methods used for PIV could be improved, namely by recording and measuring the actual error in the time domain, which would allow a less conservative estimate of the uncertainty and remove the need for the bootstrapping approach [9]. Maximum  $T_{KE}$ ,  $551\text{ m}^2\text{s}^{-2}$ , was found one cylinder diameter behind the cylinder's trailing edge, where average streamwise flow velocity was fully reversed and transverse flow velocity was near zero. The distance from the cylinder's trailing edge to the point of maximum  $T_{KE}$  is of interest for heat exchanger design [8] and the relationship between this distance,  $Re$ , and  $St$  warrants further study. Flow velocity fields from the PIV measurements were consistent with the hypothesised dipole source at the maximum  $T_{KE}$  location, and enabled a simple theoretical dipole model to be established.

The expected pressure measurements from this theoretical dipole, placed at the point of maximum  $T_{KE}$ , were compared with far-field microphone measurements obtained in the aeroacoustic wind tunnel at the University of Bristol [11]. Peak SPL = 57.5 dB was recorded at  $St = 0.18$ , which was in agreement with existing research for this  $Re$ . Mediocre agreement was found between the theoretical and experimental results, owing to an oversimplified mathematical model of acoustic wave propagation in a turbulent flow, and the chaotic nature of turbulent noise generation. In future study, a more robust theoretical model could be implemented using Lighthill's acoustic analogy [3], and a clearer understanding of the directivity of the noise source could be gained by using a beamforming approach to locate the acoustic sources in the cylinder wake [17].

Though the objective was met and the acoustic source's nature, position and orientation was determined, the observed dipole in the turbulent wake was oriented (Figure 14) such that it was unlikely to excite vibrations in the cylinder. This is evidence that VIV results from oscillating surface pressures on the cylinder as vortices are shed, rather than from acoustic waves interacting with the cylinder.

## References

- [1] J. H. Lienhard *et al.*, *Synopsis of lift, drag, and vortex frequency data for rigid circular cylinders*. Technical Extension Service, Washington State University Pullman, WA, 1966, vol. 300.
- [2] O. Reynolds, ‘Xxix. an experimental investigation of the circumstances which determine whether the motion of water shall be direct or sinuous, and of the law of resistance in parallel channels,’ *Philosophical Transactions of the Royal society of London*, no. 174, pp. 935–982, 1883.
- [3] M. J. Lighthill, ‘On sound generated aerodynamically i. general theory,’ *Proceedings of the Royal Society of London. Series A. Mathematical and Physical Sciences*, vol. 211, no. 1107, pp. 564–587, 1952.
- [4] V. Strouhal, ‘Ueber eine besondere art der tonerregung,’ *Annalen der Physik*, vol. 241, no. 10, pp. 216–251, 1878, ISSN: 0003-3804.
- [5] L. Rayleigh, ‘Xxvii. acoustical observations. ii,’ *The London, Edinburgh, and Dublin Philosophical Magazine and Journal of Science*, vol. 7, no. 42, pp. 149–162, 1879. DOI: 10.1080/14786447908639584. eprint: <https://doi.org/10.1080/14786447908639584>. [Online]. Available: <https://doi.org/10.1080/14786447908639584>.
- [6] D. Russell, J. Titlow and Y.-J. Bemmen, ‘Acoustic monopoles, dipoles, and quadrupoles: An experiment revisited,’ *American Journal of Physics*, vol. 67, pp. 660–664, 1999. DOI: 10.1119/1.19349.
- [7] R. Blevins, B. Tilden and D. Martens, ‘Vortex-induced vibration and damping of thermowells,’ *Journal of fluids and structures*, vol. 12, no. 4, pp. 427–444, 1998.
- [8] Y. N. Chen, ‘Flow-induced vibration and noise in tube-bank heat exchangers due to von karman streets,’ *Journal of Engineering for Industry*, vol. 90, no. 1, pp. 134–146, 1968, ISSN: 0022-0817. DOI: 10.1115/1.3604587. [Online]. Available: <https://doi.org/10.1115/1.3604587>.
- [9] Z. B and L. D, *Experimental methods for aerodynamics and aeroacoustics*, 2024. [Online]. Available: [www.ole.bris.ac.uk](http://www.ole.bris.ac.uk).
- [10] I. Farrance and R. Frenkel, ‘Uncertainty of measurement: A review of the rules for calculating uncertainty components through functional relationships,’ *Clin Biochem Rev*, vol. 33, no. 2, pp. 49–75, 2012, 1838-0212 Farrance, Ian Frenkel, Robert Journal Article Australia 2012/08/17 Clin Biochem Rev. 2012 May;33(2):49-75., ISSN: 0159-8090 (Print) 0159-8090.
- [11] Y. D. Mayer, H. K. Jawahar, M. Szőke, S. A. S. Ali and M. Azarpeyvand, ‘Design and performance of an aeroacoustic wind tunnel facility at the university of bristol,’ *Applied Acoustics*, vol. 155, pp. 358–370, 2019.
- [12] Y. D. Mayer, B. Zang and M. Azarpeyvand, ‘Aeroacoustic investigation of an oscillating airfoil in the pre-and post-stall regime,’ *Aerospace Science and Technology*, vol. 103, p. 105 880, 2020.
- [13] GRAS, *Gras 40pl-10 specification*. [Online]. Available: [https://www.grasacoustics.com/?eID=1709645390&import\\_id=831](https://www.grasacoustics.com/?eID=1709645390&import_id=831).
- [14] P. Welch, ‘The use of fast fourier transform for the estimation of power spectra: A method based on time averaging over short, modified periodograms,’ *IEEE Transactions on audio and electroacoustics*, vol. 15, no. 2, pp. 70–73, 1967.
- [15] I. of Sound and V. Research, *ISVR - Institute of Sound and Vibration Research*. [Online]. Available: [https://resource.isvr.soton.ac.uk/spcg/tutorial/tutorial\\_Tutorial\\_files/Web-further-dipoles.htm](https://resource.isvr.soton.ac.uk/spcg/tutorial/tutorial_Tutorial_files/Web-further-dipoles.htm).
- [16] K. Dobrosel’skii, ‘Use of the piv method for investigation of motion near a cylinder in transverse flow,’ *Journal of Engineering Physics and Thermophysics*, vol. 89, no. 3, pp. 695–701, 2016, ISSN: 1062-0125.
- [17] Y. D. Mayer, B. Zang and M. Azarpeyvand, ‘Aeroacoustic investigation of an oscillating airfoil in the pre- and post-stall regime,’ *Aerospace Science and Technology*, vol. 103, p. 105 880, 2020, ISSN: 1270-9638. DOI: <https://doi.org/10.1016/j.ast.2020.105880>. [Online]. Available: <https://www.sciencedirect.com/science/article/pii/S1270963820305629>.

## Appendices

### A Uncertainties

The uncertainty in Welch's method is associated with the statistical convergence error, and is inversely proportional to the square root of the number of segments used for the evaluation [9]. Pressure measurements were recorded at a sampling frequency  $f = 2^{16}\text{Hz}$  for 10 s, so the total number of data points is  $10 \times 2^{16}$ . The Hanning window for Welch's method was chosen as  $2^{13}$ , resulting in  $10 \times 2^3$  segments. With an overlap of 90 %, the number of segments is multiplied by 10, resulting in a total number of segments and a statistical error:

$$n_{\text{segments}} = 100 \times 2^3 = 800 \quad (\text{A-1})$$

$$\text{error}_{\text{Welch}} = \frac{1}{\sqrt{n_{\text{segments}}}} \simeq 0.035 = 3.5\% \quad (\text{A-2})$$

Then, following the rules for uncertainty propagation in [10, Equation 15], the SPL error is estimated as:

$$\text{error}_{\text{SPL}} = 2 \times \frac{1}{\text{error}_{\text{Welch}}} \times \log_{10} e \simeq 0.030 = 3\% \quad (\text{A-3})$$

For the  $T_{KE}$  uncertainties, Equation (2) must be inspected. It can be shown that:

$$\text{error}_{u^2} = 2 \times \text{error}_u = 6\% \quad (\text{A-4})$$

thus, if  $\text{error}_{u^2} = \text{error}_{v^2}$  then the percentage error does not change when  $u^2$  and  $v^2$  are summed together. This is one of our assumptions: that the error is the same in both directions. In reality, there is likely a higher error in the streamwise direction due to the faster flow speed, but this was ignored for analysis as the initial error estimate was conservative.

### B Microphone Data

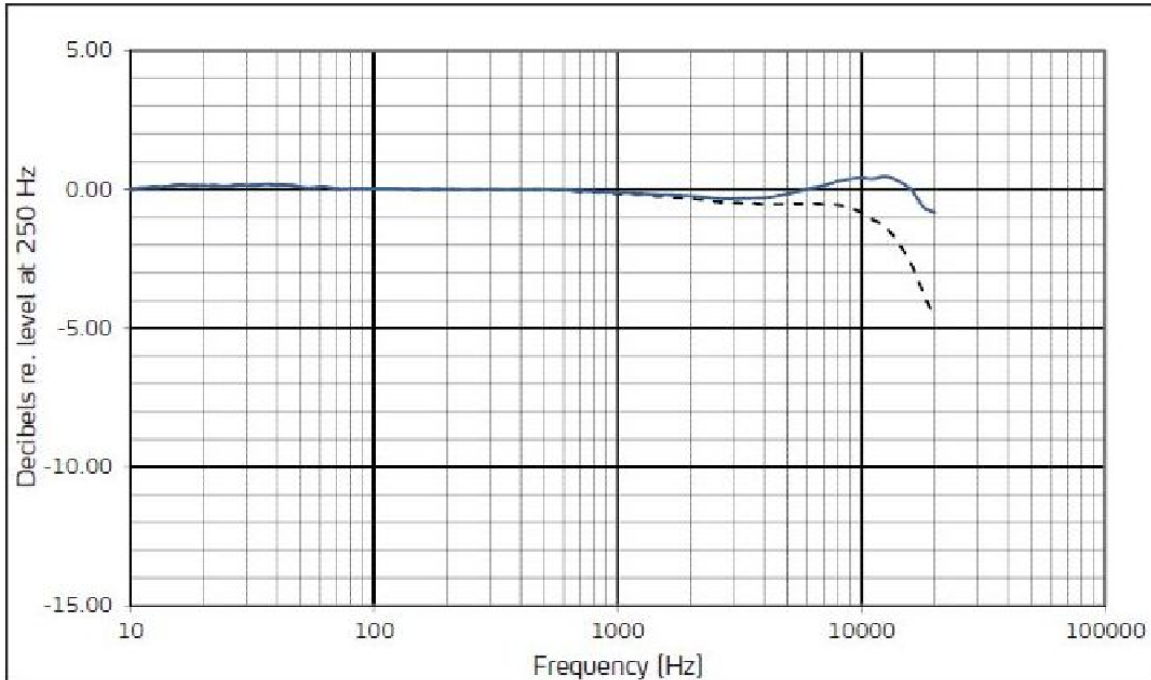


Figure B-1: Microphone Frequency Response from the manufacturer [13]

### C Ideal Dipole Geometry

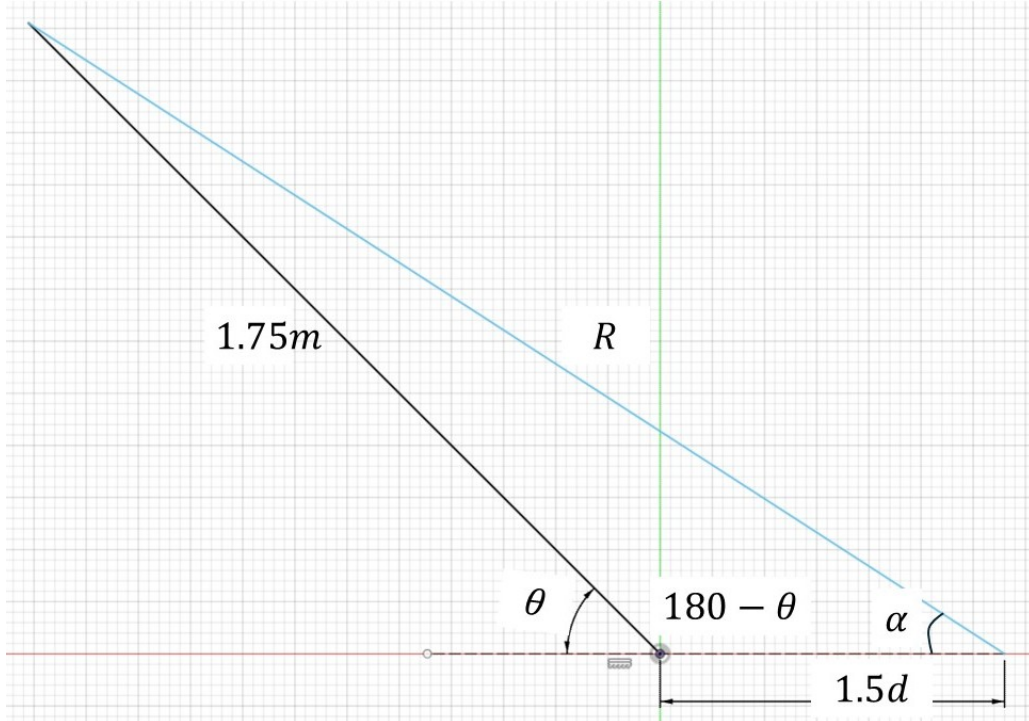


Figure C-2: [NOT TO SCALE] Diagram of Dipole Radius Calculation

The microphone array was centred on the cylinder, so a correction must be applied to accurately model the distance and angle of each microphone from the dipole sound source, which was observed to be a few mm behind the cylinder's trailing edge. Figure C-2 shows how the theoretical radius for Equation (6) was calculated based on the angle of the microphone, the known distance to the microphone array, and the measured distance of maximum  $T_{KE}$ . Maximum  $T_{KE}$  occurs 22 mm behind the trailing edge, or  $1.5d$  behind the centre of the cylinder, where  $d$  is the cylinder diameter. Since the angle  $\theta$  is known, a simple cosine rule can be used to calculate the unknown side length,  $R$  which is then used as the value for  $r$  in Equation (6), along with the angle  $\alpha$  being used for the microphone direction:

$$R^2 = 1.75^2 + 1.5^2 d^2 - 2 \cdot 1.75 \cdot 1.5d \cdot \cos(180 - \theta) \quad (\text{C-5})$$

Importantly, this does not account for the speed of the nozzle exit as it is only  $M \simeq 0.07$  so only a small perturbation is expected. This simple model is vulnerable to distortion and dissipation from the turbulence made by the jet mixing with the stagnant far field at the nozzle exit.